Fabrication of a symmetric micro supercapacitor based on tubular ruthenium oxide on silicon 3D microstructures

Xiaofeng Wang*, Yajiang Yin, Xiangyu Li, Zheng You

Department of Precision Instrument, Tsinghua University, No. 1 Tsinghuayuan, Haidian District, Beijing, PR China

HIGHLIGHTS

- We have fabricated a micro supercapacitor with 3D microelectrode processed through ICP technique.
- Hydrous ruthenium oxide with tubular morphology is successfully synthesized by means of the cathodic deposition technique.
- "Grassy micro prominence" on surface of Si arrays is believed to be micro template for cathodic electrodeposition process.
- Specific geometric capacitance and gravimetric capacitance of microelectrode reach 99.3 mF cm^{-2} and 70 F g^{-1}, respectively.
- Specific geometric capacitance of micro supercapacitor reach 23 mF cm^{-2}.

ARTICLE INFO

ABSTRACT

A micro-supercapacitor with a three-dimensional configuration has been fabricated using an ICP etching technique. Hydrous ruthenium oxide with a tubular morphology is successfully synthesized using a cathodic deposition technique with a Si micro prominence as a template. The desired tubular RuO$_2$·xH$_2$O architecture facilitates electrolyte penetration and proton exchange/diffusion. A single MEMS electrode is studied using cyclic voltammetry, and a specific capacitance of 99.3 mF cm^{-2} and 70 F g^{-1} is presented at 5 mV s^{-1} in neutral Na$_2$SO$_4$ solution. The accelerated cycle life is tested at 80 mV s^{-1}, and satisfactory cyclability is observed. When placed on a chip, the symmetric cell exhibits good supercapacitor properties, and a specific capacitance as high as 23 mF cm^{-2} is achieved at 10 mA cm^{-2}. Therefore, 3D MEMS microelectrode arrays with electrochemically deposited ruthenium oxide films are promising candidates for on-chip electrochemical micro-capacitor applications.

1. Introduction

The rapid development of micro-electro-mechanical systems (MEMS) and microelectronics enables the miniaturization of systems. Microsystems with integrated sensors, actuators and control circuits have been used in various areas, such as the automotive and microelectronics industries, as well as space exploration, biomedical research and healthcare [1]. In these applications, micro-batteries [2] are the leading potential power sources, while other candidates [3] continue to emerge, such as miniaturized solar [4] and mechanical vibration energy harvesters [5]. However, the limited life span of micro-batteries is a major problem when these batteries must be integrated into inaccessible systems where maintenance and replacement are impossible. In addition, micro-batteries are ineffective during low temperature or high power applications, such as wireless transmission. Micro-supercapacitors can be paired with either micro-batteries to enhance their peak power and cycle lifetime or energy harvesting devices to store the generated energy. Moreover, micro-supercapacitors with a high energy density can work as stand-alone and maintenance-free power sources during numerous applications.

Recent efforts in the micro-supercapacitor field have focused on increasing the energy and power densities by improving the material properties and architecture of the devices [6–11]. Most of the reported micro-supercapacitors have a shared platform of inter-digital electrodes. Activated carbon powder was ink jet-printed on inter-digital gold current collectors by Pech et al. [12], producing micro-supercapacitors with a 27 mF cm^{-2} geometric capacitance. Jiang fabricated a double layer supercapacitor utilizing vertically aligned 80-µm-high carbon nanotube forests on silicon

* Corresponding author. Tel.: +86 10 62776000; fax: +86 10 62782308.
 E-mail addresses: xfw@tsinghua.edu.cn, xfw@mail.tsinghua.edu.cn (X. Wang).

wafers, generating a capacitance density of 428 μF cm^{-2} and a power density of 0.28 mW cm^{-2} [13]. Xue fabricated solid-state electrochemical micro-supercapacitors using photolithography, electrochemical polymerization and solution casting techniques [14]. Sun reported the electrochemical fabrication of three-dimensional (3D) polypyrrole (PPy) electrode architectures for micro-capacitors with a geometric capacitance and a specific power of 29 mF cm^{-2} and 2.2 mW cm^{-2}, respectively [15].

Three-dimensional (3-D) architectures offer new approaches for miniaturized power sources. These micro devices are designed to have a small footprint while providing power and energy density sufficient for operating autonomous MEMS devices and micro-electronic circuits. Beidaghi developed activated C-MEMS structures for micro-supercapacitor applications [16]. These micro-capacitors presented specific capacitances up to 75 mF cm^{-2} at 5 mV s^{-1} after electrochemical activation. The energy density of this micro-capacitor was further improved by conformally coating PPy on the C-MEMS structures [17]. The electrochemical characterizations revealed that these micro-capacitors could deliver a specific capacitance of approximately 162.07 mF cm^{-2} at 20 mV s^{-1}. The recent advances in the design and fabrication of on-chip micro-supercapacitors were comprehensively reviewed by Beidaghi and Wang [18].

There are a few reports in the literature regarding micro-supercapacitors containing ruthenium oxide pseudo-capacitive materials. Liu revealed micro-supercapacitors with hydrous RuO_2 interdigital electrodes that exhibited a specific capacitance of 10.5 mF cm^{-2} at 50 mV s^{-1} [19]. However, the capacitance in the studies mentioned above dropped quickly at higher scan rates. The high internal resistance and limited surface area of the planar electrode caused this behavior. Arnold employed laser direct write and micromachining to fabricate high capacity hydrous ruthenium oxide micro ultracapacitors [20]. The specific capacitance of the laser-deposited materials was comparable to reported values of 720 F g^{-1}. Sugimotoa synthesized the RuO_x electrodes by electrodeposition using a lyotropic liquid crystal template method [21]. The ordered mesoporous RuO_x on an inter-digitated array electrode afforded specific capacitance of 400 F g^{-1}. Pt@RuO_2 core shell nanotube arrays were prepared by electrodepositing RuO_2 on Pt nanotubes and evaluated as micro-supercapacitor electrodes by Ponrouch [22]. The specific geometric capacitance for the RuO_2 core shell nanotube electrodes was 320 mF cm^{-2} at 2 mV s^{-1} and 256 mF cm^{-2} at 500 mV s^{-1}, thus demonstrating the high utilization factor of RuO_2 due to the facilitated proton and electron transport. Hydrous RuO_2 nanotubular array electrodes were synthesized using an anodic deposition technique by Hu [23]. The specific power and energy density of the annealed $RuO_2 \cdot H_2O$ nanotubes were 4320 kW kg^{-1} and 7.5 Wh kg^{-1}, respectively, revealing the characteristics of next-generation micro-supercapacitors.

This study introduces a different approach toward improving the energy and power density of micro-capacitors by combining a Si MEMS current collector with a high surface area and a pseudo-capacitive ruthenium oxide film with a high capacitance. The inductively coupled plasma (ICP) etching and focused-ion-beam method (FIB) techniques were used to fabricate 3D current collectors for micro-supercapacitors. The ruthenium oxide was electrochemically deposited on the pre-etched MEMS arrays to generate a pseudo-capacitive micro cell. This research employed the "grassy prominence" phenomenon for the first time; this distinctive behavior arises during the ICP etching of Si MEMS used as the template for growing the pseudo-capacitive film. A ruthenium oxide film with a unique tubular appearance was electrodeposited on the above-mentioned structure and studied in detail for the first time. Cyclic voltammetry and galvanostatic charge–discharge

experiments were conducted to evaluate the electrochemical performance of both a single microelectrode and entire symmetric cells. Utilizing a microstructure in the 3D current collector improved the charge storage properties and the cycle life of ruthenium oxide-based micro-supercapacitors.

2. Experimental

2.1. Design of the micro-supercapacitor

Fig. 1 provides the schematic and processing flow of an MEMS supercapacitor with a 3D structure. It contains a Si structure with a 3D configuration, a layer of SiO_2, a conformal Au layer for the current collector and a continuous layer of electro-active ruthenium oxide. The total footprint area of a typical 3D electrode is 2 × 2 mm and contains 832 pillars that are 50 μm in diameter. The distance between the centers of adjacent pillars is 75 μm, and the pillars are 80 μm high. Structuring and fabricating the electrodes in a 3D configuration generates a higher effective surface area in the device footprint compared to thin film or 2D interdigital electrodes. The fabrication process can be summarized as follows: Step 1 involves etching the silicon substrate with integrated 3D structures using ICP. Step 2 involves applying Au on the surface of the Si substrate via conformal radio-frequency (RF) sputtering. Step 3 involves etching a deep electrical isolation trench using FIB. Step 4 involves conformally electrodepositing ruthenium oxide on the surface of the metallic layer.

2.2. Fabrication of 3D MEMS structures

This experiment applied the BOSCH ICP process. The detailed procedure for fabricating 3D structures was as follows: first, a 200-nm-thick Al layer was deposited on a cleaned Si substrate using RF sputtering under a 100% Ar atmosphere at room temperature. Afterward, the Al layer was structured in a side-by-side pattern using photolithography and wet etching for use as an ICP protection mask. Furthermore, the high-aspect-ratio ICP process was carried out with an STS LPXICP ASE - SR (Britain) to form the 3D structure, while using SF_6 as the etching gas and C_4F_8 as the passivation gas. After removing the Al mask, the conformal SiO_2 layer was formed as an insulator using thermal oxidation. Next, traditional RF sputtering was used to deposit the conformal Au current collectors on the surface with an FHR MS 100X6-L (German). Finally, FIB was carried out with a ZESS FIB/SEM AURIGA (German) in a mediate position to avoid contact (short circuit) between the two microelectrodes.

2.3. Preparation of ruthenium oxide films

Electrodeposition was used to add the ruthenium oxide film to the 3D MEMS Si/Au samples. The two electrodes in each device were connected, and the device was used as the working electrode in an electrochemical cell. Platinum wires served as the reference and counter electrodes. Ruthenium oxide was deposited on the MEMS current collectors using an electrolyte solution containing 5 mmol L^{-1} $RuCl_3$ and 200 mmol L^{-1} $NaNO_3$ at 500 mA cm^{-2} for 500–2000 s. The film prepared was rinsed and dried at 100 °C for approximately 30 min. To remove the effect of leakage current on calculation for capacitance of single electrode, all samples were subjected to cyclic voltammetric charge/discharge with a scan rate 80 mV s^{-1} for more than 200 cycles prior to other experimental investigations. The mechanism for the formation of RuO_2 from the $RuCl_3 \cdot nH_2O$ precursor is very complicated. The hydrated ruthenium chloride is a heterogeneous ionic material with an average ruthenium oxidation state between 3 and 4 [24,25]. Cathodic

electrosynthesis is similar to the wet chemical method used during amorphous oxide powder processing, using an electrogenerated base instead of alkali [26,27]. During RuO_2 preparation starting from $RuCl_3 \cdot nH_2O$ via electrosynthesis, the 3+ metal ions should be oxidized to 4+ ions [28]. This process and oxidation of the minor metallic Ru phase in the fresh deposit increases the sample weight due to the oxygen uptake. Electrosynthesis enables not only the production of ruthenium oxide but also its deposition onto a complex substrate. The X-ray and TG analyses reveal that the deposits contain significant amounts of an amorphous and hydrous phase with remarkable capacitive energy storage properties [25]. Moreover, 100 °C was the optimal treatment temperature. Higher temperatures can cause excessive crystallization and water loss, leading to decreases in capacity. For the sake of simplicity, $RuO_2 \cdot xH_2O$ is used to represent the functional film on surface of the microstructure in the following text. Similarly, a planar electrode with nearly an equal amount of loading was fabricated using identical electrodeposition on a smooth Au/Si substrate within the same footprint as the 3D structure. The surface topography and electrochemical performance of the film were also investigated for comparison.

2.4. Characterization

Cyclic voltammetry (CV) and galvanostatic charge/discharge (GCD) were used to investigate the electrochemical performance of the 3D and planar electrodes. Every electrochemical test was carried out on a potentiostat/galvanostat (660B, CHI instrument, China) using both three-electrode and two-electrode systems in 0.1 mol L^{-1} aqueous Na_2SO_4 electrolyte. In the three-electrode system, a single micro electrode served as the working electrode, while a Pt sheet and a saturated calomel electrode (SCE) were the counter and reference electrodes, respectively. In the two-electrode system, two MEMS electrodes served as the working and the counter electrodes, respectively. All the potentials in the following text are based on the reference voltage for SCE. The microstructure and surface topography of the MEMS electrodes were studied using a scanning electron microscope (SEM FEI, Sirion 200, Netherlands). The energy dispersive spectra (EDS) were also used to characterize
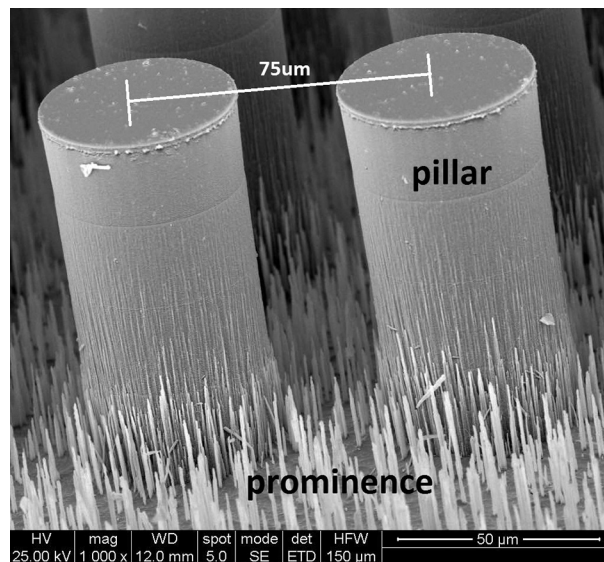

Fig. 2. The surface topography of 3D microstructures with a large "black silicon phenomenon" area.

the electro active layer on the 3D Au/Si surface. An X-ray diffractometer was used to characterize the crystalline structure of the electrodes. X-ray diffraction (XRD) patterns of the samples were obtained using a Cu K radiation system (60 kV, 80 mA, Bruker AXS D8 discover, German).

3. Results and discussion

3.1. SEM imaging and XRD pattern

The surface topography of the three-dimensional silicon microstructure is presented in Fig. 2. A broad area containing the "black silicon phenomenon" that is usually blamed for bad figures during ICP processes was prepared on a silicon wafer.
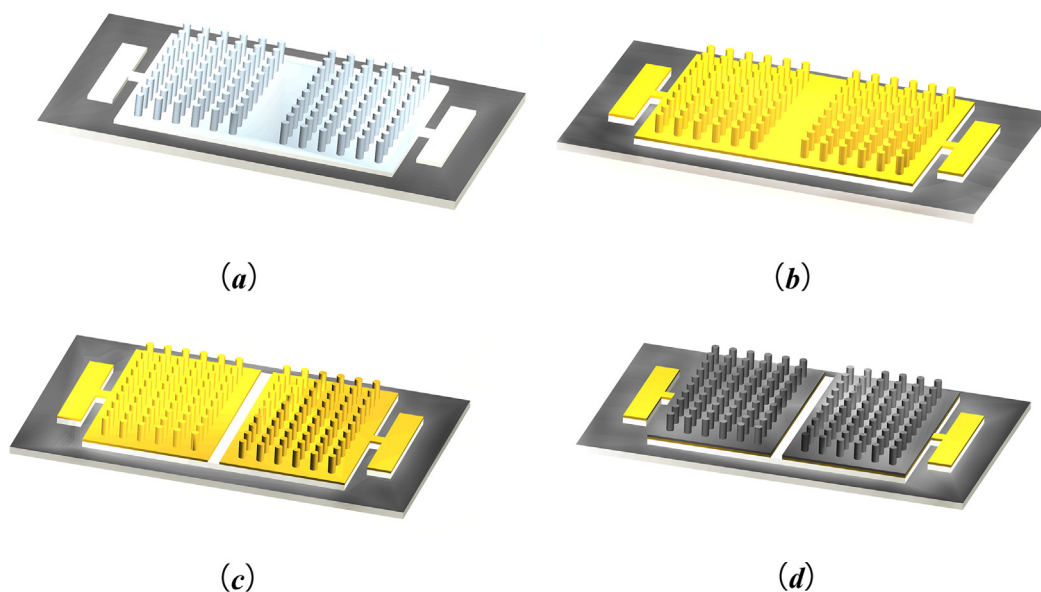

Fig. 1. A proposed structure and processing flow for fabricating the 3D micro-supercapacitor. (a) Step 1: fabricating the 3D structure using ICP. (b) Step 2: fabricating the Au layer on arrays via RF sputtering. (c) Step 3: fabricating the isolation trenches with FIB. (d) Step 4: fabricating the active film using electrodeposition.
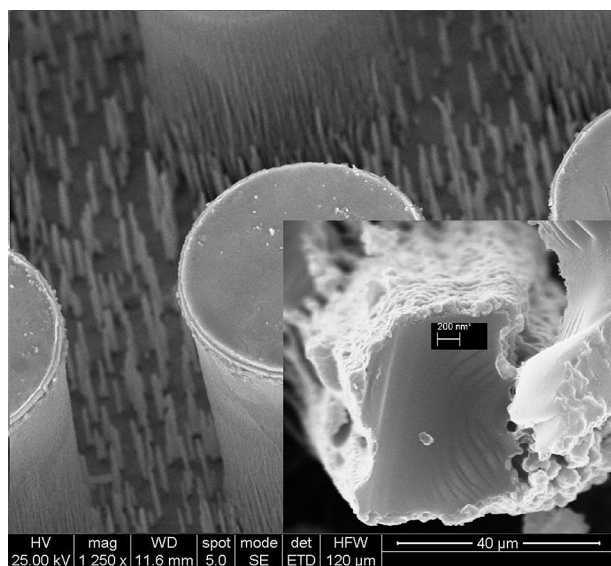
Fig. 3. SEM image of ruthenium oxide electrodeposited for 500 s.

Consequently, the "grassy prominence" phenomenon appeared at the base of the pillar arrays. A special process was observed during the ruthenium oxide electrodeposition onto those micro prominences, and the distinctive tubular topography is shown in Figs. 3 and 4. The detailed electrodeposition procedure could be divided into two periods. During the earlier period, the active material climbed the pillar and micro prominence. The details of a separate silicon prominence are shown in Fig. 3: a broken prominence was covered with a conformal film layer. During the later period, the film continued growing to almost entirely cover the silicon prominence. The tubular microstructure grew vertically at the foot of the pillars, as shown in Fig. 4. Notably, the active material growth along the silicon prominence remained uninterrupted, and the scaly appearance of these films was unusual. The only difference between the above two topographies was that the

microstructure obtained during the second period was cylindrical and hollow. The tubular frame shown in Fig. 4 represented the continued deposition oxide film around the silicon prominence; this feature can be treated as a micro template for electrodeposition. For comparative study, SEM micrographs of electrochemically deposited ruthenium oxide on a planar electrode surface are shown in Fig. 5. The irregular formed $RuO_2 \cdot xH_2O$ materials were unevenly electrodeposited with obvious fractures. The desired schematic structure for the growth process of tubular structure in Figs. 3 and 4 is explicitly illustrated in Fig. 6. The EDS observations in Fig. 7 indicate that the tubular structure is mainly composed of elemental oxygen and ruthenium. The effect of the deposition time (500 s for Fig. 7a and 2000 s for Fig. 7b) on the properties of the $RuO_2 \cdot xH_2O$ films was studied. The atomic ratio of Ru and O was about 1:2 and oxygen content increased gradually over time. The crystalline structures of electrochemically deposited ruthenium oxide were characterized using an X-ray diffractometer as shown in Fig. 8. The X-ray diffraction pattern of 3D electrode with oxide film showed no diffraction peaks for $RuO_2 \cdot xH_2O$ film electrodeposited at temperature lower than 100 °C, but peaks which were corresponding to the Au/Si substrate were obtained. These results indicate that at lower annealing temperatures, the electrodeposited $RuO_2 \cdot xH_2O$ was in an amorphous phase. Consequently, the cylindrical hollow structure should be important for improving the capacitive characteristics of $RuO_2 \cdot xH_2O$-based microsupercapacitors. The special electrochemical effects inherent to this distinctive tubular structure will be discussed in the following text.

3.2. Electrochemical testing of a single electrode

The capacitive properties of the materials can be revealed using cyclic voltammetry. The CV curves for the 3D and planar microelectrode with the same formation charge of 40C (0.02 A × 2000 s) are shown in Fig. 9. It should be noted these two electrodes were of an identical size of 0.2 × 0.2 cm². For comparison, the normalized current density (i.e., faradic current divided by the footprint area of the electrode) is used as a vertical axis in the normalized CV plots instead of the current. A significant difference appeared in the
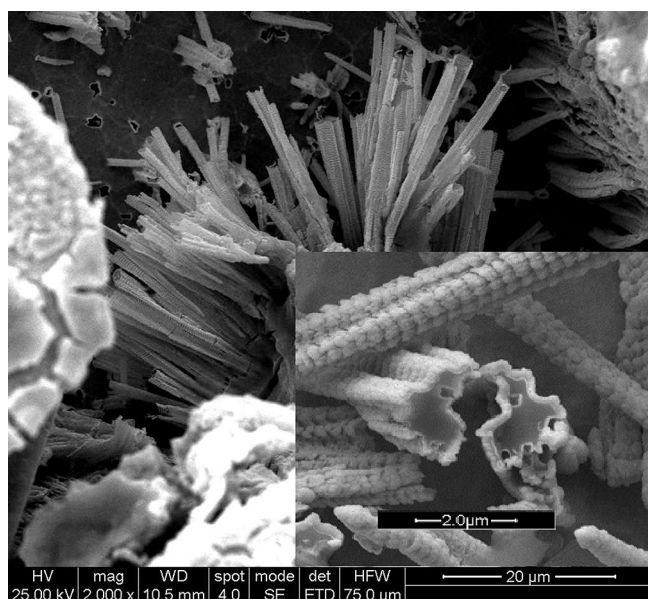

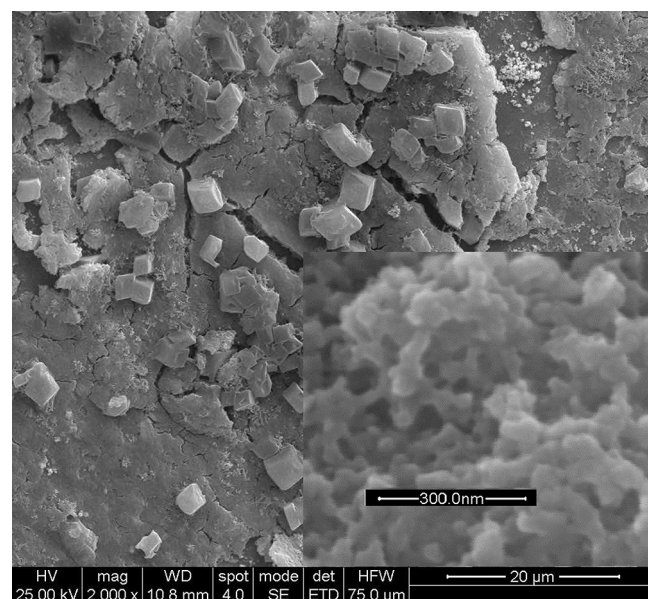**Fig. 4.** SEM image of ruthenium oxide electrodeposited for 2000 s.

Fig. 5. SEM image of ruthenium oxide electrodeposited on a planar electrode.
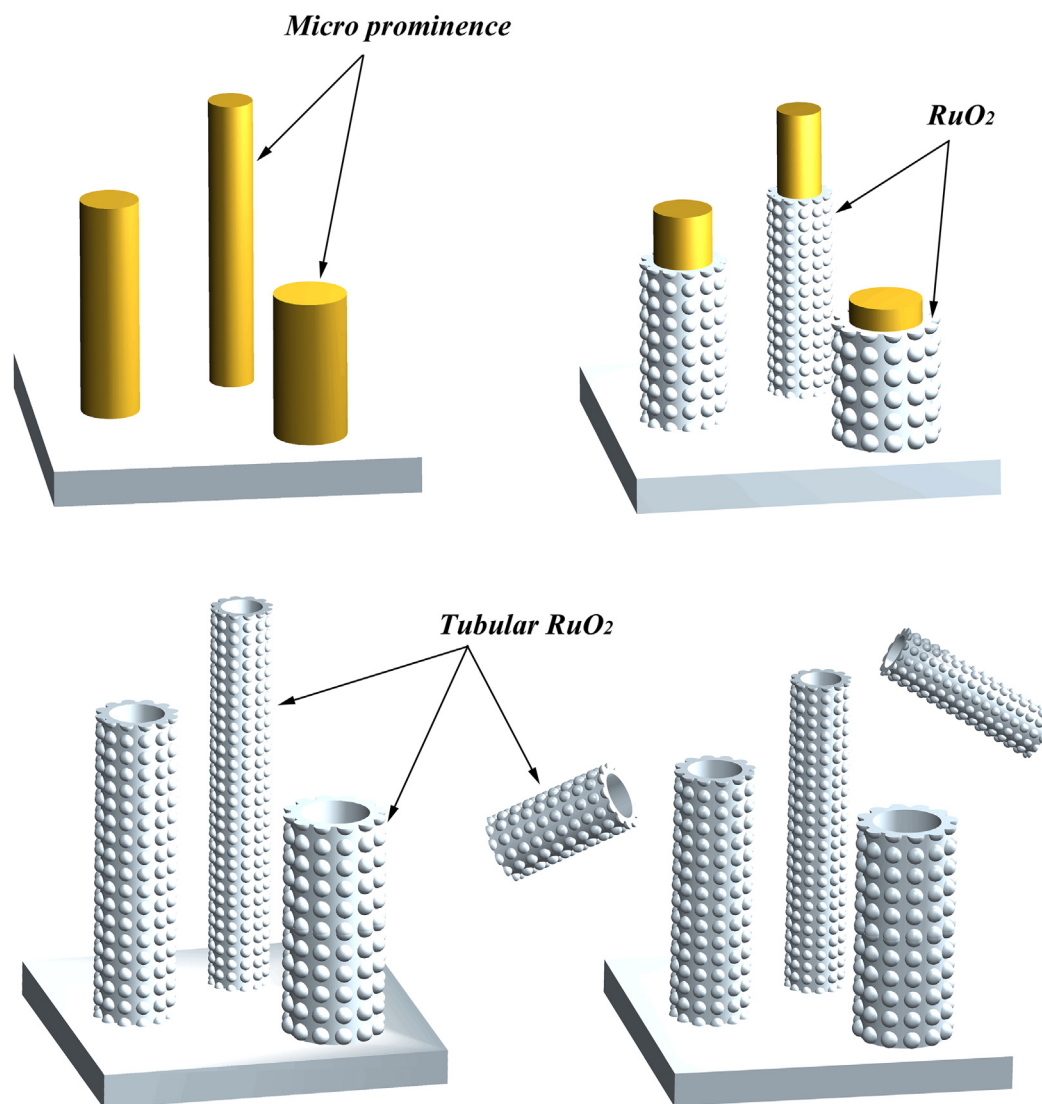
Fig. 6. Desired schematic structure for growing tubular ruthenium oxide.

redox responses during the cyclic voltammetry experiments with the planar and 3D electrodes. As shown in Fig. 9a, the 3D electrode exhibited a pseudocapacitive behavior and the redox features derived from the valence changes in ruthenium can be observed at 0.2−0.4 V vs. SCE. In contrast, the CV response of the planar electrode had an asymmetric character at 20 mV s^{-1}. The current response for the planar electrode was a little smaller than that for the 3D electrode. This is due to the fact that 3D electrode designed and fabricated has more surface area compared to the planar one. At much higher scan rate of 200 mV s^{-1}, the CV curve for the 3D electrode remained regular quadrilateral as shown in Fig. 9b, and this shape is an indication of ideal capacitive behavior. Moreover, the area enclosed by the 3D sample's CV curve was significantly larger than that of the planar sample, implying that 3D "grassy prominence" structure can be utilized as highly effective surface area current collectors for nanostructured ruthenium oxide films. The proton can permeate through the bulk of the amorphous $RuO_2 \cdot xH_2O$ much easily.

In addition, we assume that a hollow, tubular structure can act as a reservoir and channel for the electrolyte, while the porous $RuO_2 \cdot xH_2O$ architecture facilitates electrolyte penetration/diffusion. Moreover, the hydrous nature of $RuO_2 \cdot xH_2O$ enhances the rate of proton exchange because the superficial redox transitions in $RuO_2 \cdot xH_2O$ involve a proton and electron double injecting/expelling process [24,25]. The desired schematic structure for a tubular $RuO_2 \cdot xH_2O$ electrode in a micro-supercapacitor is shown in Fig. 10. The tubular $RuO_2 \cdot xH_2O$ provides an electron "high-speed channel" for charge storage and delivery. Consequently, the networked $RuO_2 \cdot xH_2O$ tube structure decreases the ion intercalation distance to the nanometer range, facilitates the charge-transfer and reduces the resistance over time.

While all the results reported above were obtained in Na_2SO_4 solution, Fig. 11 shows for 3D electrode the comparison between the voltammetric curves at 20 mV s^{-1} in 0.1 mol L^{-1} Na_2SO_4 and in 6 mol L^{-1} H_2SO_4 electrolyte. The curves differ in two respects: (1) In H_2SO_4 electrolyte, the CV curve presents non-ideal capacitance character and hydrogen evolution is observed down to −0.3 V vs. SCE. While in Na_2SO_4 electrolyte, the 3D electrode performs ideal capacitance property with rectangle-like shape. (2) The reactive current density is much higher for electrode in Na_2SO_4 electrolyte.
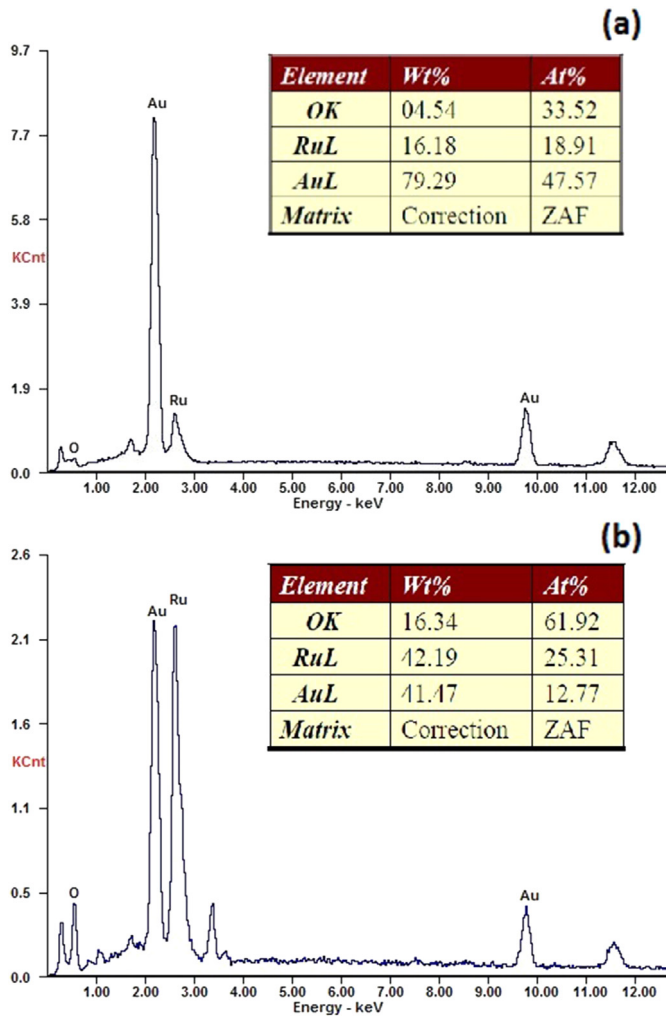
Fig. 7. The EDS of ruthenium oxide electrodeposited for 500 s (a) and 2000 s (b).

It was also found that the CV characteristic of $RuO_2 \cdot xH_2O$ was insensitive to the concentration of Na_2SO_4. In consideration of strong corrosive effect of sulfuric acid, Na_2SO_4 solution is confirmed as "preferred electrolyte" in this paper.
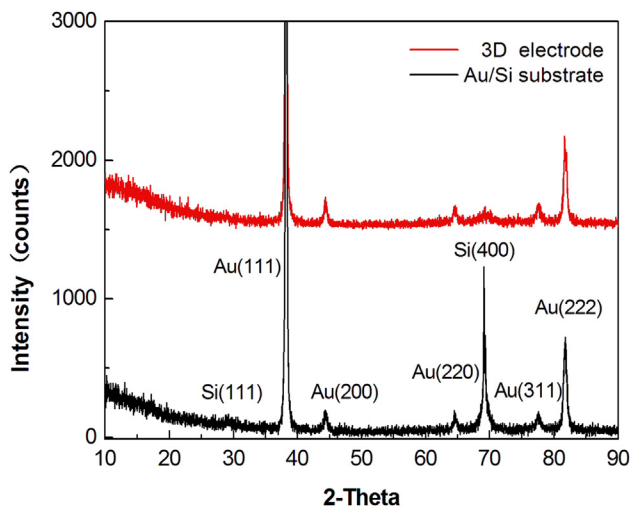

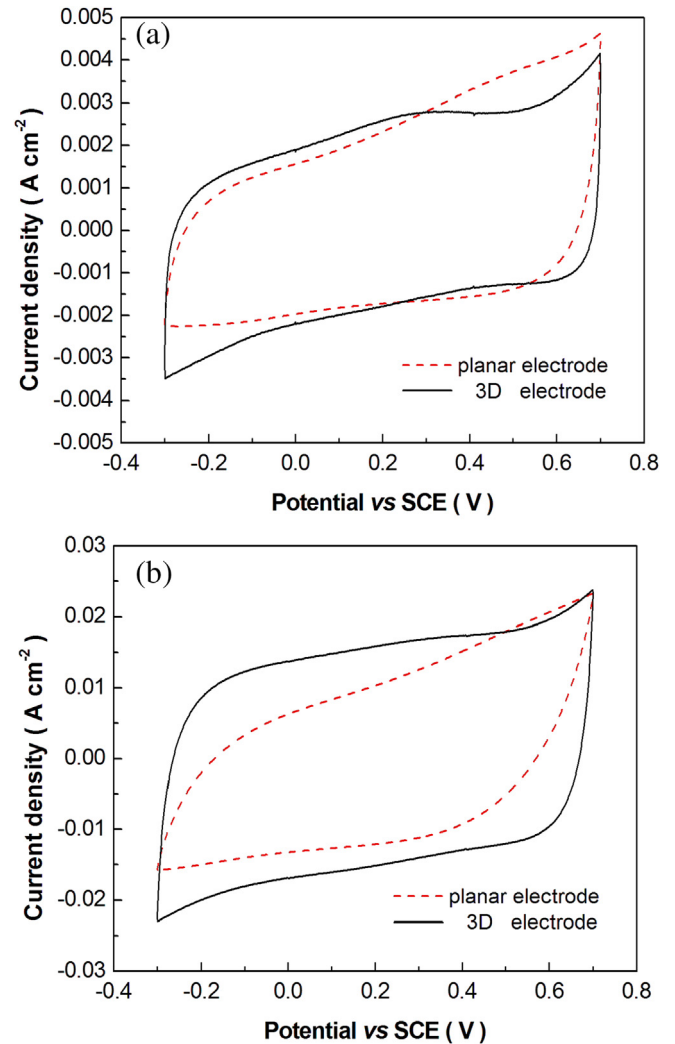Fig. 8. X-ray diffraction patterns for Ruthenium oxide prepared on 3D electrode.

Fig. 9. Cyclic voltammograms of the 3D microelectrode (solid line) and the planar microelectrode (dashed line) at scan rate of 20 mV s^{-1} (a) and 200 mV s^{-1} (b).

The capacitance of a single electrode can be calculated by integrating the current of CV curves in discharge half cycle according to Eq. (1):

$$C = \frac{\int I(V)\mathrm{d}V}{S \cdot \Delta V} \tag{1}$$

where $\int I(V)\mathrm{d}V$ is the total voltammetric charge obtained by integrating the negative sweep in the cyclic voltammograms, S is the scan rate, and ΔV is the width of the potential window. To calculate the specific gravimetric and geometric capacitance of each electrode, eqs. (2) and (3) have been used respectively.

$$C_m = \frac{C}{m} \tag{2}$$

$$C_A = \frac{C}{A} \tag{3}$$

where C is the capacitance of the single electrode, C_m is the specific gravimetric capacitance and m is the mass, C_A is the specific geometric capacitance and A is the geometric area of a single electrode. Fig. 12 presents the CV curves for a single 3D microelectrode
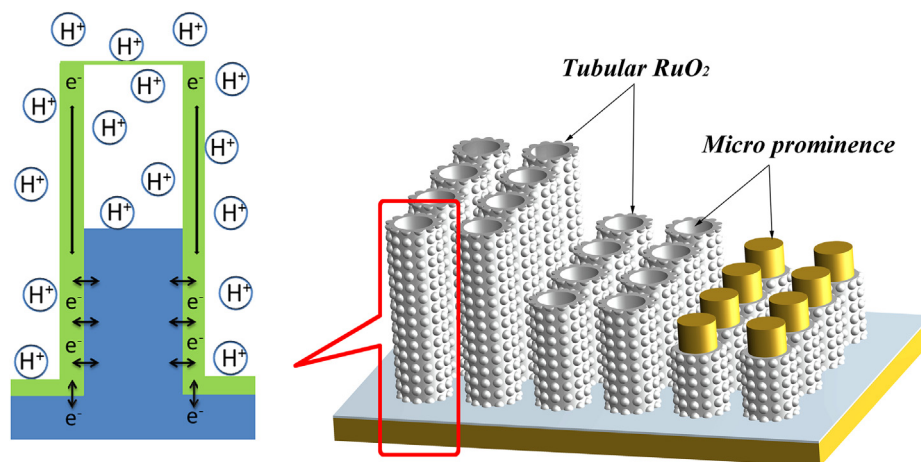
Fig. 10. Desired schematic structure for the tubular $RuO_2 \cdot xH_2O$ microstructure applied in a micro-supercapacitor.

electrodeposited at scan rates from 5 to 500 mV s^{-1}. The reversible and rectangular behavior is also observable for CV recorded at 500 mV s^{-1}, revealing the excellent proton and electron transport in the 3D electrode. The primary reason for this has been discussed above. The specific geometric capacitances and gravimetric capacitance at different scan rates were deduced using the CV data and are shown in Fig. 13. The highest value for the geometric capacitance (99.3 mF cm^{-2}) is measured at the lowest scan rate (5 mV s^{-1}). At this scan rate, the gravimetric capacitance and volumetric capacitance (geometric capacitance divided by the height of pillars) is calculated as 76 F g^{-1} and 12.4 F cm^{-3}, lower than reported value in literature [20,21]. The geometric capacitance of the 3D electrode drops rapidly (from 99.3 to 80.1 mF cm^{-2}) when the scan rate increases from 5 to 100 mV s^{-1} and decreases much more slowly (from 80.1 to 58.5 mF cm^{-2}) when the scan rate ranges from 100 to 500 mV s^{-1}. The explanation for above phenomenon is straightforward. At slow scan rates, the proton diffusion process finishes over a long interval, resulting in a large capacitance, while at a fast scan rate, the charge diffusion cannot follow the fast scan rate, thus generating a smaller geometric capacitance [15]. The specific capacitance of a planar microelectrode is also presented in Fig. 13 for comparison. Although the highest value (81.9 mF cm^{-2} and 60 F g^{-1}) for the planar system is also found at the lowest scan

rate (5 mV s^{-1}), the specific capacitances of the planar electrode are significantly lower at higher scan rates, demonstrating the effective utility of $RuO_2 \cdot xH_2O$ due to its facilitation of proton and electron transport in the 3D electrode.

The two types of microelectrodes were also examined using CV tests over 1500 cycles in the three-electrode system. The accelerated cycle life was tested at 80 mV s^{-1}; this value is large in the context of microelectrodes. The capacitance values are plotted and shown in Fig. 14. The specific capacitance of this 3D sample during the 200th cycle was approximately 74 mF cm^{-2}. It can be seen that the capacitance decreased briefly within the next 100 cycles. Within 300 to 1500 cycles, the capacitance held roughly steady. After 1500 cycles, the specific capacitance was 70.4 mF cm^{-2}. A 4.8% decrease was observed relative to the initial capacitance, revealing the reliable cyclability of electrodeposited 3D microelectrodes, particularly in view of the high power settings used during this experiment. For comparison, the initial value of planar sample during the 200th cycle was about 64 mF cm^{-2}. The capacitance decreased about 12% within the next 500 cycles. Within 700 to 1500 cycles, the capacitance decayed at a much slow rate and the ultimate value for was 56.8 mF cm^{-2}. To some extent, the better cyclability of the 3D sample is attributed to the network of Si micro
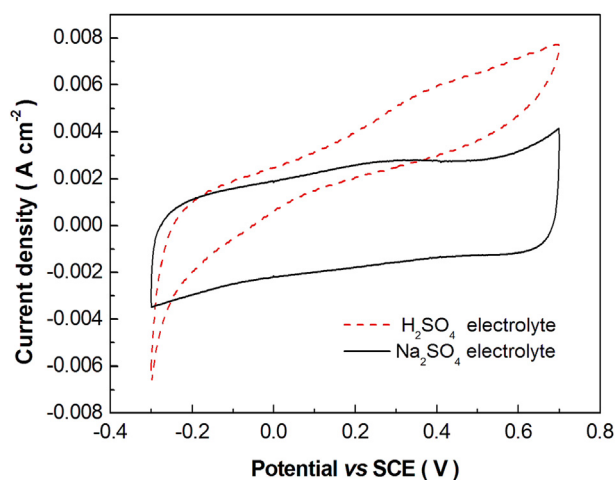

Fig. 11. Cyclic voltammograms (20 mV s^{-1}) of 3D microelectrode in 0.1 mol L^{-1} Na$_2$SO$_4$ electrolyte (solid line) and 6 mol L^{-1} H$_2$SO$_4$ electrolyte (dashed line).

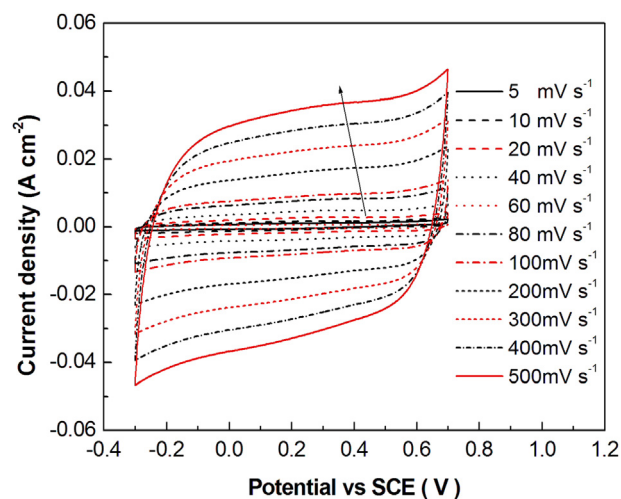**Fig. 12.** Cyclic voltammogram of the 3D microelectrode in 0.1 M Na$_2$SO$_4$ at sweep rates from 5 to 500 mV s^{-1} (the arrow indicates the direction of the increasing scan rate).
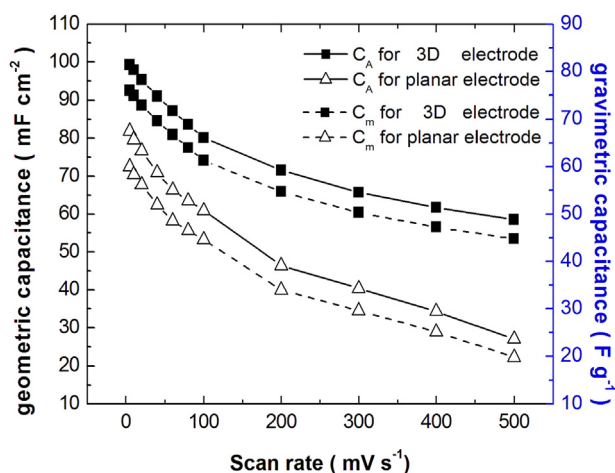
Fig. 13. The specific geometric (solid line) and gravimetric (dash line) capacitance of two types of electrode at various scan rates.

prominences that effectively impede the breakdown of the film, similar to a reinforcing bar in concrete, as shown in Fig. 3.

3.3. Electrochemical cell tests

The symmetric supercapacitor consisted of two 3D microelectrodes that were electrodeposited for 2000 s; this device was tested with a two-electrode system in 0.1 mol L^{-1} Na$_2$SO$_4$. The two electrodes on one chip had identical design specifications; they were fabricated simultaneously. To investigate the performance of a cell containing two identical electrodes, galvanostatic charge/discharge experiments were performed using various current densities over a voltage range of 0–1.0 V. Charge–discharge cycles of symmetric micro-supercapacitors are presented in Fig. 15. The curves show a triangular shape with linear charge and discharge half cycles, typical of supercapacitors. From the Fig. 15, the energy deliverable efficiency can be easily estimated from the capacity ratio between discharge and charge processes and is over 92%.

The geometric capacitance of a cell can be calculated using linear sections of discharge curves according to Eq. (4):
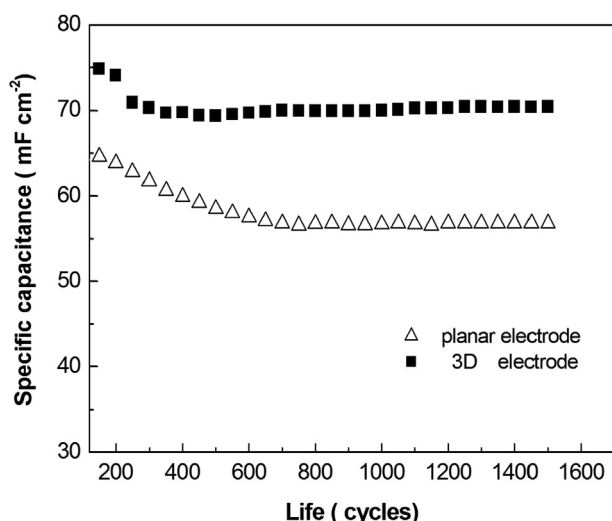

Fig. 14. Cyclic performance and capacity retention for the 3D and planar electrodes.
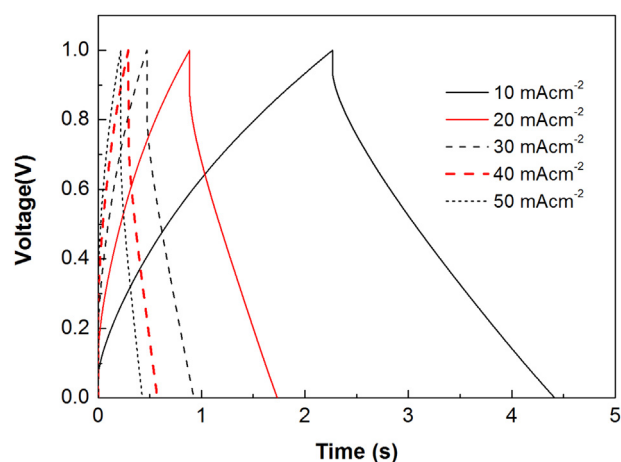

Fig. 15. Galvanostatic charge and discharge curves for a cell composed of two 3D electrodes with various discharge rates.

Table 1
Variations in the capacitance of a micro-supercapacitor at different discharge rates.

Current (mA)	Current density (mA cm^{-2})	Discharge time (s)	Specific capacitance (mF cm^{-2})	Average specific power (mW cm^{-2})
0.2	2.5	11.1	28.4	1.3
0.4	5.	5.00	26.4	2.6
0.8	10	2.12	23.0	5.4
1.2	15	1.25	21.0	8.4
1.6	20	0.75	17.3	11.5
2.0	25	0.60	18.1	15.1
2.4	30	0.45	16.9	18.8
2.6	32.5	0.39	16.4	20.8
2.8	35	0.35	15.9	22.8
3.2	40	0.28	15.2	27.5
3.6	45	0.23	14.9	31.8
4.0	50	0.21	14.5	37.0

$$C = \frac{I \cdot \Delta t}{\Delta V \cdot A} \qquad (4)$$

where I is the discharge current, A is the area of the cell (twice the size of single electrode), t is the discharge time, and ΔV is the potential window after the iR drop.

The average specific power (P) of the cell can be calculated using Eq. (5):

$$P = \frac{E}{\Delta t} = \frac{0.5C(\Delta V)^2}{\Delta t} \qquad (5)$$

where E is the specific energy density of the cell. The specific capacitances (C) and the specific powers (P) at different current densities are shown in Table 1. The average specific capacitance decreases and the specific power increases as the current density increases from 2.5 to 50 mA cm^{-2}. The specific capacitance for a cell is in general consistent with the expected value from the specific capacitance of a single electrode. The specific capacitance was 23 mF cm^{-2}, and the specific power density was 5.4 mW cm^{-2} at 10 mA cm^{-2}, which is a relatively large discharge rate. Utilizing 3D current collectors can improve the performance of a device with a limited footprint at a high rate discharge.

4. Conclusion

This paper describes a novel method for fabricating a 3D micro-supercapacitor on silicon substrates using ICP technology.

Ruthenium oxide films with distinctive tubular topography are successfully constructed using cathodic electrodeposition. This unique structure not only reduces the diffusion resistance of electrolytes but also enhances ion transportation. The special "grassy prominence" microstructures that are typically observed during ICP processes on silicon substrates enhance the growth process for the pseudo-capacitive film. The electrochemical characterization of the electrochemically deposited microelectrodes reveals their excellent capacitive behavior. A specific geometric capacitance of 99.3 mF cm^{-2} was achieved after cathodic deposition occurred for 2000 s. The performance of a micro-supercapacitor containing two identical electrodes was investigated electrochemically in a Na$_2$SO$_4$ solution. The specific capacitance (23 mF cm^{-2}) and the specific power density (5.4 mW cm^{-2}) were obtained. MEMS techniques, such as ICP, are very promising methods for fabricating micro-supercapacitors.

Acknowledgments

References

[1] T. Masako, Microelectr. Eng. 84 (2007) 1341–1344.
[2] J.F.M. Oudenhoven, R.J.M. Vullers, R. Schaijk, Int. J. Energy Res. 36 (2012) 1139–1150.
[3] H.B. Radousky, H. Liang, Nanotechnology 23 (2012) 1–35.
[4] J.L. Cruz-Campa, G.N. Nielson, P.J. Resnick, Progr. Photovolt. 21 (2013) 1114–1126.
[5] S.G. Kim, S. Priya, I. Kanno, MRS Bull. 37 (2012) 1039–1050.
[6] C.W. Shen, X.H. Wang, S.W. Li, J. Power Sources 234 (2013) 302–309.
[7] B. Hsia, M.S. Kim, M. Vincent, Carbon 57 (2013) 395–400.
[8] H. Durou, D. Pech, D. Colin, Microsyst. Technol. Micro-Nanosyst. Inf. Storage Process. Syst. 18 (2012) 467–473.
[9] J. Ren, L. Li, C. Chen, Adv. Mater. 25 (2013) 1155–1159.
[10] W.W. Liu, X.B. Yan, J.T. Chen, Nanoscale 5 (2013) 6053–6062.
[11] D. Pech, M. Brunet, M.D. Ty, J. Power Sources 230 (2013) 230–235.
[12] D. Pech, M. Brunet, P.L. Taberna, J. Power Sources 195 (2009) 1266–1269.
[13] Y. Jiang, P. Wang, J. Zhang, et al., in: 2010 IEEE 23rd International Conference on Micro Electro Mechanical Systems (MEMS), Hon Kong, China, 24–28 January, 2010.
[14] M.Q. Xue, Mianqi, Z. Xie, L.S. Zhang, Nanoscale 3 (2011) 2703–2708.
[15] W. Sun, R. Zheng, X. Chen, J. Power Sources 20 (2010) 7120–7125.
[16] M. Beidaghi, W. Chen, C.L. Wang, J. Power Sources 196 (2011) 2403–2409.
[17] M. Beidaghi, C.L. Wang, Electrochim. Acta 56 (2011) 9508–9514.
[18] M. Beidaghi, C.L. Wang, in: Conference on Energy Harvesting and Storage – Materials, Devices, and Applications III, Baltimore, Maryland, 23–24, April, 2012.
[19] C.C. Liu, D.S. Tsai, D. Susanti, et al., Electrochim. Acta 55 (2010) 5768–5774.
[20] C.B. Arnold, R. Wartena, K.E. Swider-Lyons, A. Pique, J. Electrochem. Soc. 150 (2003) A571–A575.
[21] S. Makino, Y. Yamauchi, W. Sugimoto, J. Power Sources 227 (2013) 153–160.
[22] A. Ponrouch, S. Garbarino, E. Bertin, D. Guay, J. Power Sources 221 (2013) 228–231.
[23] C.C. Hu, K.H. Chang, M.C. Lin, Y.T. Wu, Nano Lett. 6 (2006) 2690–2695.
[24] Zhitomirsky, L. Gal-Or, Mater. Lett. 31 (1997) 155–159.
[25] Zhitomirsky, Mater. Lett. 33 (1998) 305–310.
[26] Zhitomirsky, A. Kohn, L. Gal-Or, Mater. Lett. 25 (1995) 223–227.
[27] J.P. Zheng, T.R. Jow, J. Electrochem. Soc. 142 (1995) L6–L8.
[28] M. Guglielmi, P. Colombo, V. Rigato, G. Battaglin, A. Boscolo-Boscoletto, A. De Battisti, J. Electrochem. Soc. 139 (1992) 1655–1661.